Gelatin-derived N-doped hybrid carbon nanospheres with an adjustable porous structure for enhanced electromagnetic wave absorption

Xiaoke Lu[1] · Dongmei Zhu[1] · Xin Li[2] · Minghang Li[2] · Qiang Chen[1] · Yuchang Qing[1]

Abstract

Eco-friendly biomass-derived absorbers with high electromagnetic wave (EMW) absorbing property are ideal substitutes for traditional carbon absorber coming from non-renewable fossil energy. Based on this, a kind of novel gelatin-derived N-doped hybrid carbon nanospheres with adjustable porous structure (PGCNs) was fabricated successfully in this work by a simple desolvation method and following alkaline-activation process. By assembling precursor macromolecule to endow carbon absorber with unique tailored structure, the unstable EMW absorption performance caused by the unreproducible morphologies of most natural biomass precursors can be well avoided. Moreover, the developed porous structure on PGCNs could be tuned by changing the alkaline addition, following by the optimization of EMW absorbing performance. When loaded with 15 wt.%, the minimum reflection coefficient (RC_{min}) of PGCNs could reach as low as −58.03 dB at the thickness of merely 1.9 mm. The effective absorption bandwidth (EAB) was up to 6.3 GHz at the thickness of 2.2 mm. This work puts forward a new inspiration for designing repeatable structure for biomass-derived carbonaceous materials, and we believe that the as-fabricated PGCNs could be potential candidates in future EMW absorbing application.

1 Introduction

With the increasing popularization of diverse electronic equipment, electromagnetic pollution is an urgent problem to solve, following by explosive progress in the studies of electromagnetic wave (EMW) absorbers [1–5]. However, with the development of industrialization, applications in harsh working conditions such as humid and corrosive environment put forward higher requirements to electronic equipment and EMW absorbing materials. Most existing traditional material types cannot meet these higher demands. For example, although with excellent loss capacity, absorbers containing magnetic (e.g., Co [6], Fe [7], Fe_3O_4 [8], and CoNi [9–11]) and semiconductor materials (e.g., SnO_2 [12], MoS_2 [13], and ZnO [14, 15]) both inevitably suffer from shortcomings such as high density and low anti-oxidant/corrosion ability. In order to avoid these problems, rational design on the nanostructure of pure carbonaceous absorbers seems to be more effective, not only because of their low density and high resistance to chemical corrosion, many studies have proved that porous nanostructures with high specific surface area may contribute to lower density and higher EMW absorbing capability by strengthening polarization loss (related to large heterogeneous interfaces) and multiple reflection/scattering [1, 15–17].

As a renewable, low-cost, and resource-rich carbon precursor, biomass carbon has received significant attention in EMW absorbing fields [15, 18]. Many biomass precursors possess unique naturally formed structures, which could convert into carbon materials by the facile carbonization process and exhibit excellent EMW absorbing performance. However, these structures formed in the growing process would take a very long time and restricted in unchangeable morphologies. Hence, the optimal structure design via regular geometry and tunable porosity of biomass carbon is

✉ Qiang Chen
chenqiang0213@126.com

[1] State Key Laboratory of Solidification Processing, School of Materials Science and Engineering, Northwestern Polytechnical University, Xi'an 710072, China

[2] Science and Technology On Thermostructural Composite Materials Laboratory, Northwestern Polytechnical University, Xi'an 710072, China

an efficient method to achieve great improvement on EMW absorbing properties. Lately, Liu et al. [48] synthesize porous carbon aerogel using gelatin, which possess a bandwidth of 6.6 GHz (2.5 mm) and a reflection loss of −61.7 dB (2.6 mm), indicating the important role about structural design. However, low filler loading and thin thickness are still formidable challenges for absorbers. At the same time, methods commonly reported for constructing geometric structure usually limited to template-etching method (involving hydrofluoric acid [20]) and hydrothermal reaction [19], both of which possess security threat to researchers and even in future application. To solve these problems, exploring facile method to endow biomass precursor with high specific area/low density is necessary.

Herein, porous gelatin-derived carbon nanospheres (PGCNs) with tunable morphology were successfully prepared via a convenient desolvation method followed by an alkaline-activation process. The first step is to assemble gelatin macromolecule into uniform nanospheres; the second step is to simultaneously carbonize and construct tunable porous structure on the absorbers by the activation of alkali. A porous spherical structure with high specific area could be regulated by simply changing the addition content of KOH. Compared with regular biomass-derived absorbers, the as-prepared PGCNs present some advantages not only including synergistic effects of various loss mechanisms and well-matched characteristic impedance but also excellent controllability and reproducibility. Our findings introduce a new way to transform gelatin into nanoscale porous carbon spheres, which provide a facile strategy to the application of biomass carbon and give inspiration to other biomass-derived absorbers.

2 Experimental section

2.1 Raw materials

Potassium hydroxide (KOH), hydrochloric acid (HCl), acetone, and glutaraldehyde aqueous solution (GA, 25% *v/v*) were bought from Sinopharm Co. Ltd. Gelatin Type-B was bought from Sigma-Aldrich, USA.

2.2 Experiment procedure

2.2.1 Synthesis of GNs

The method to synthesize gelatin nanospheres (GNs) is a two-step desolvation method [21], and the formation mechanisms of GNs are shown in Supplementary Information. Briefly, gelatin solution (50 *g/L*) and acetone were mixed with a volume ratio of 1:1 to obtain macromolecule precipitation. The precipitation was then redissolved, and the pH

was adjusted to 2. With continuous magnetic stirring, the solution would become turbid after being dropped acetone. GA was added for crosslinking. The dry GNs powder was obtained after wash and lyophilization.

2.2.2 Synthesis of PGCNs

The synthesized GNs were pretreated at 200 °C for complete dehydration. This intermediate was then pre-carbonized at 500 ℃ for 2 h in a vacuum furnace, and the product was named as gelatin-derived carbon nanospheres (GCNs). After that, the GCNs powder was fully soaked with proper KOH and deionized water overnight. The mixture was finally calcinated at 800 °C with the protection of N_2 to form porous gelatin-derived carbon nanospheres (PGCNs). The specific value of GCNs: KOH was changed to 1:2, 1:3, 1:4, and 1:5; the PGCNs were denoted as PGCNs-2, PGCNs-3, PGCNs-4, and PGCNs-5, accordingly. For subsequent comparison, the GCNs were also carbonized at 800 °C without activation process, and the sample was marked as PGCNs-0. In addition, the GCNs were activated at 700 and 900 °C to explore the influence of activation temperature, and the samples were denoted as PGCNs-3–700 and PGCNs-3–900, respectively. The schematic illustration of the preparation process of PGCNs is shown in Fig. 1.

2.3 Characterization

The morphology of testing samples was observed by scanning electron microscopy (SEM; Helios G4 CX, FEI, USA) and transmission electron microscopy (TEM; Talos F200X, 200 kV, FEI, USA) equipped with energy-dispersive X-ray spectroscopy (EDS). The crystalline structure and phase compositions were tested by Raman spectra (RMS; Renishaw, UK) with a He–Ne laser ($\lambda = 532$ nm) and X-ray diffraction (XRD; Rigaku-D/max-2400, Tokyo, Japan) radiation. The surface status was characterized by X-ray photoelectron spectroscopy spectra (XPS; iN10MX, Nicolet, USA). Nitrogen adsorption–desorption curves were tested by Micromeritics ASAP2010 equipment. The Brunauer–Emmett–Teller (BET) method was used to calculate the specific surface area (SSA). The pore size distribution was calculated by the Barrett-Joyner-Halenda (BJH) method.

2.4 The dielectric measurement and calculation

To investigate the EMW absorbing performance of the as-obtained PGCNs absorbers, the relative complex permittivity within 2–18 GHz was tested by coaxial method (Agilent Technologies E8362B). Paraffin was chosen as matrix material due to its characteristic of wave transmission. The testing samples containing 15 wt.% of PGCNs were pressed into toroidal pipes. Paraffin was dissolved into hexane and

Fig. 1 Schematic of the fabrication process of PGCNs
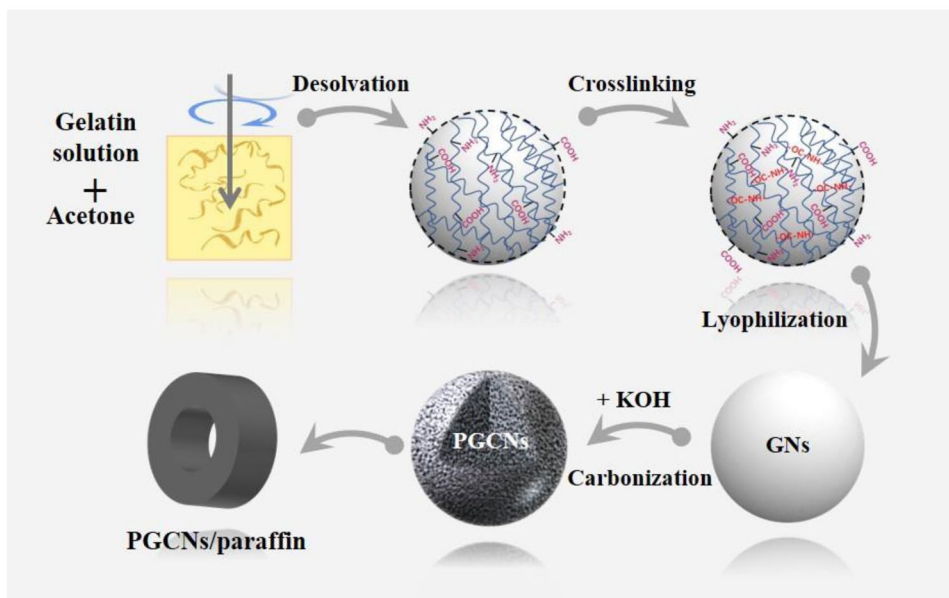
grinded with the PGCNs, and the mixture was blended by ultrasonic dispersion method to get homogeneous dispersion. The reflectivity coefficient (RC) is the key factor to evaluate EMW absorbing performance of absorbers, which can be simulated on the basis of transmission line theory [22–25]. The equations are as follows:

$$RC = 20lg\left|\frac{Z_{in} - Z_0}{Z_{in} + Z_0}\right| \tag{1}$$

$$Z_{in} = \sqrt{\frac{\mu_r}{\varepsilon_r}}tanh\left[j(\frac{2f\pi d}{c})\sqrt{\mu_r\varepsilon_r}\right] \tag{2}$$

where Z_{in} is the input impedance, Z_0 is air impedance, f is frequency, d is the thickness of the samples, c is the velocity of light, and ε_r and μ_r are the relative complex permittivity and permeability, respectively.

3 Results and discussion

With the activation effect of KOH, the pre-carbonized gelatin will decompose into escaping gases such as H_2O, CO and CO_2, which contribute to the formation of porous structure on absorbers [15, 24]. The generated pores can provide the paths for the gas mixture to escape from the carbon base exactly during the carbonization process. The detailed reaction process can be described as follows:
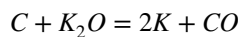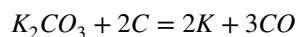
$$6KOH + 2C = 2K + 3H_2 + 2K_2CO_3$$

$$K_2CO_3 = K_2O + CO_2$$

$$CO_2 + C = 2CO$$

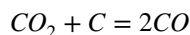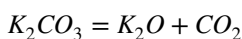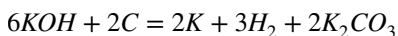$$K_2CO_3 + 2C = 2K + 3CO$$

$$C + K_2O = 2K + CO$$

Figure 2 a–f show the SEM images of GNs and PGCNs absorbers. It can be seen from Fig. 2a that the precursor GNs present uniform spherical morphology, and the particle sizes are ~ 200 nm, relatively uniform, and consistent. After being carbonized, the PGCNs-0 (Fig. 2b), PGCNs-2 (Fig. 2c), and PGCNs-3 (Fig. 2d) samples still maintain their original spherical structure. When compared with PGCNs-0, the activation of KOH did not destroy the whole spherical morphology of PGCNs-2 and PGCNs-3, but makes their surface gradually rough, indicating the generation of pores. When increasing the amount of activator, the roughness of the surface becomes obvious. However, when the GCNs: KOH ratio is up to 1:4, the intact sphere begins to break, and some visible holes appear on the surface of absorbers, which may be because of the over intense generation of gases. For the same reason, the morphology of PGCNs-5 shows a microstructure of deformed spheres, indicating the structural collapse caused by excessive KOH. The TEM images of PGCNs-0 and PGCNs-3 are shown in Fig. 2 g and h respectively. Without the activating function of KOH, PGCNs-0 presents a completely spherical structure. Its edge is relatively smooth, indicating the flat surface of the carbon absorber. In contrast, the PGCNs-3 exhibits a quite rough and porous morphology, which may be formed by the etching effect of KOH. The element distribution of PGCNs-3 was manifested by EDS as shown in Fig. 2i, four images all

Fig. 2 SEM images of **a** GNs, **b** PGCNs-0, **c** PGCNs-2, **d** PGCNs-3, **e** PGCNs-4, and **f** PGCNs-5. TEM images of **g** PGCNs-0 and **h** PGCNs-3. **i** EDS element mapping images of PGCNs-3; HRTEM images (inset of **g**), and SAED images (inset of **h**)
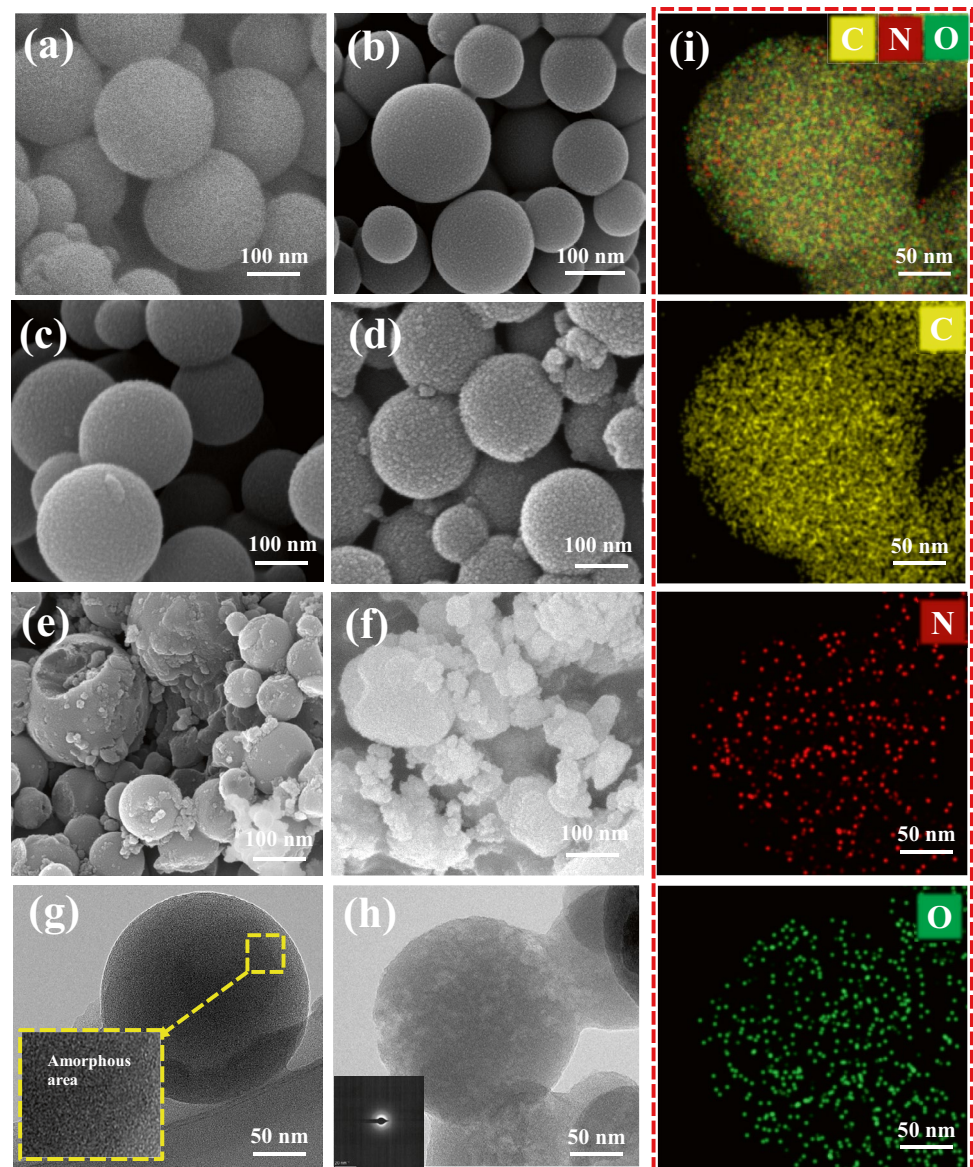
correspond to Fig. 2h, and three different colors represent C, O, and N elements, respectively. After the decomposing process of carbonization and activation, naturally doped N, O elements are still reserved evenly within the PGCNs. The HRTEM and SAED images demonstrate the amorphous state of samples.

N_2 adsorption–desorption isotherm is recorded to analyze the porous properties of PGCNs. The SSA, total pore volume (V_{pore}), and average pore size are shown in Table S1. As shown in Fig. 3a, N_2 adsorption–desorption curves of all the PGCNs present a similar variation trend when the relative pressure from 0.0 to 1.0 is assigned to the type I isotherm. Four curves all show a rapid rise at low relative pressure region ($P/P_o < 0.2$), and then a gradual increase kept during the rest of relative pressure range (P/P_o up to ~0.8), and finally following with a slight hysteresis loop

gradually caused by mesopores, which indicates the coexistence of micro-/mesopores in PGCNs [26, 27]. The BJH pore size distribution results also evidence the existence of nanopores less than 10 nm. The SSA of PGCNs-2 and PGCNs-4 increased from 1704.4 to 2106.7 $m^2 \cdot g^{-1}$, as well as the obviously increased pore volume (from 0.0253 to 0.4798 $cm^3 \cdot g^{-1}$) and pore size (from 2.71 to 3.48 nm), which indicate that the increasing addition of KOH does play an important role on the formation of nanopores and inside PGCNs. However, the overuse of KOH leads to the decreasing of SSA, pore volume, and average pore size of PGCNs-5, which is attributed to the collapse and breakage of porous spherical structure as indicated in SEM images (Fig. 2e, f).

The XRD patterns of the PGCNs are shown in Fig. 3b. There are two broad diffraction peaks at ~25° and ~44°,
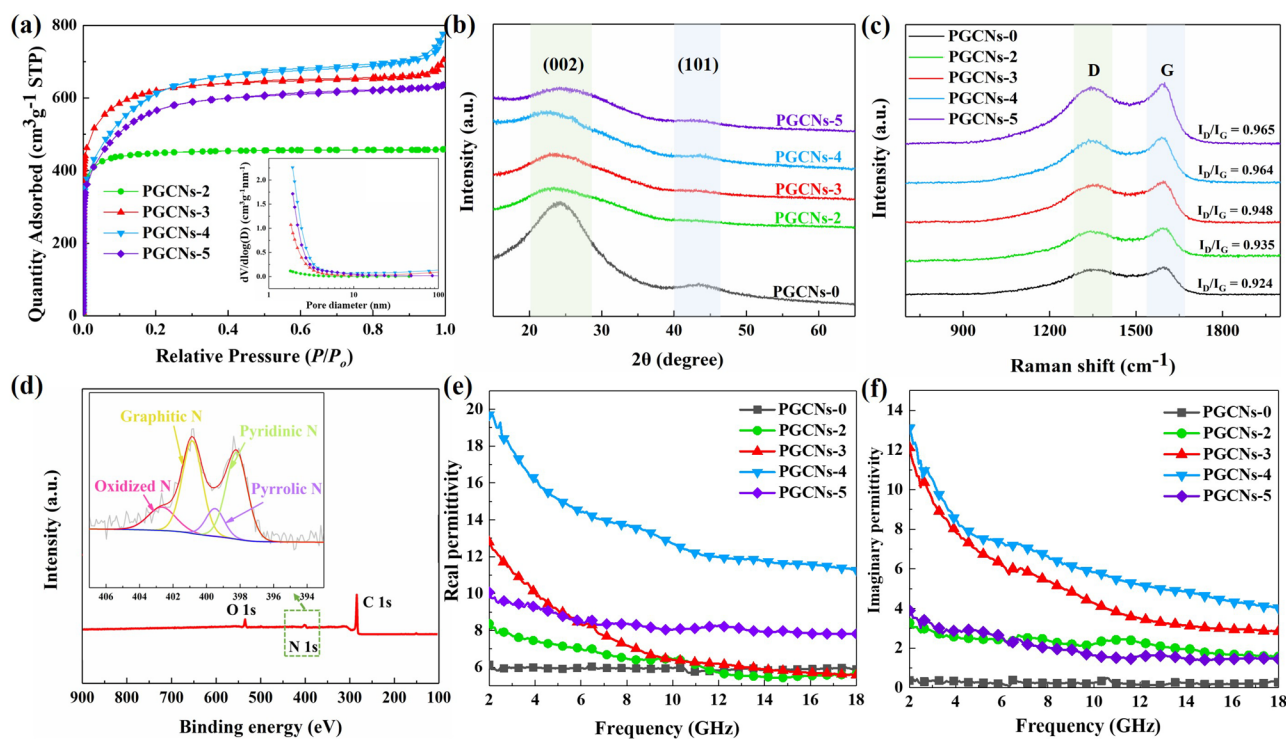
Fig. 3 **a** N_2 adsorption–desorption curve and pore size distribution, **b** XRD patterns, **c** Raman spectra of PGCNs-0, PGCNs-2, PGCNs-3, PGCNs-4, and PGCNs-5. **d** Full XPS spectrum and high-resolution on N 1s of PGCNs-3; real part **e** and imagine part **f** of complex permittivity values of PGCNs-0, PGCNs-2, PGCNs-3, PGCNs-4, and PGCNs-5

corresponding to (002) and (101) of carbon, respectively [20]. The peak at ~ 25° implies the amorphous region of materials; the peak at ~ 44° indicates the ordered lattice region of carbon, implying the amorphous state of all the prepared samples, which is consistent with the HRTEM images above. Due to the enlarging destructive effect on graphitic crystalline structure from gradually increasing activation, PGCNs-2, PGCNs-3, PGCNs-4, and PGCNs-5 samples exhibit much weaker peaks than PGCNs-0. Raman spectra were to investigate the chemical state of the samples (Fig. 3c). Two peaks at ~ 1340 and ~ 1590 cm^{-1} correspond to D and G peak. The graphitization degree of carbonaceous materials is generally estimated by the ratio of I_D to I_G [19, 28]. The I_D/I_G of five samples are 0.924, 0.935, 0.948, 0.964, and 0.965, respectively, implying that all the samples have quite low degree of graphitization and similar bonding state of carbon atoms. The slightly increasing I_D/I_G of PGCNs may result from the generation of defects after being activated, which is consistent with the previous variation trend exhibited in SEM images, N_2 adsorption–desorption curves, and XRD patterns.

To explore the element chemical state of PGCNs, XPS spectrum of PGCNs-3 was exhibited. The full spectrum (Fig. 3d) reveals three characteristic peaks, indicating the presence of C, N, and O, corresponding with results of

previous EDS (Fig. 2i). The O 1s and C 1s peaks can be divided into four peaks [29] and two peaks [30] respectively (Fig. S1a-b). The N 1s peak can be mainly fitted into four peaks at 398.3 eV, 400.1 eV, 400.9 eV, and 402.6 eV, assigned to pyridinic N, pyrrolic N, graphitic N, and oxidized N, respectively (larger version in Fig. 3d) [31]. The incorporation of pyridinic N and pyrrolic N can raise the conductivity because of the nature of their electron donors. The existence of these four N doping forms can also lead to the non-coincidence of charge centers, forming a dipole under the effect of electromagnetic fields and consuming electromagnetic energy through dipole polarization to improve the dielectric loss upon EMW irradiation [32], which can be realized easily in carbon absorber derived from biomass, no extra element introducing step is required.

EMW absorbing performance of non-magnetic absorbers is highly correlated with their complex permittivity (real parts and imaginary parts of complex permeability are regarded as 1 and 0, including the real parts (ε') and the imaginary parts (ε''), representing the storage capability of electric energy and the loss capability of electric energy, respectively [33]. In this work, the complex permittivity of paraffin-matrix samples with 15 wt.% PGCNs loading was measured during 2–18 GHz; the results are exhibited in Fig. 3e, f. With the frequency increasing, the values of ε'

range from 6.1 to 5.9, 8.4 to 5.6, 12.8 to 5.6, 19.7 to 11.3, and 10.0 to 7.8 for PGCNs-0, PGCNs-2, PGCNs-3, PGCNs-4, and PGCNs-5, respectively. The decrease of each ε' value could be attributed to frequency dispersion behavior [24, 34]. With the increasing ratio of KOH, PGCNs-4 sample shows the largest ε' value, indicating the strongest storage ability of electric energy. At the same time, the ε'' shows similar changing tendency with ε'. Both PGCNs-4 and PGCNs-3 samples exhibit higher value than the other three samples, indicating relatively excellent electric dissipation capability. The sample PGCNs-0 exhibits lowest value on ε' and ε'', which is almost independent from the frequency value, predicting its poor contribution on the dissipation of EMW. For carbonaceous materials, the values of complex permittivity are generally related with their graphitization degree, which is depending on the carbonization temperature. However, in this study, the graphitization degree of all the samples is quite similar, not only because of the consistent carbonization temperatures according to the experiment schedule but also the proof provided by previous analysis about Raman spectra. Therefore, the change of microstructure should be the major factor for the complex permittivity changing. Compared with other samples, PGCNs-3 and PGCNs-4 samples exhibit higher SSA and more defects induced by KOH, which means larger carbon (solid)-air (void) nano-interfaces. Under the action of electromagnetic field, charges will accumulate at the carbon-air interface and then contribute to the increase of complex permittivity in the form of interfacial polarization loss [25, 35]. In addition, under the alternating electromagnetic field, microcurrent could be formed on such conductive network thereby enhancing conductive loss [19, 24]. Besides, nanopores on such carbon skeleton can be understood as capacitor-like structure, which also contribute to the conductive loss [24]. Different porous structure caused by the KOH activation will directly affect the conductive network of the material. With the same mass fraction, the volume fraction and conductive form of the absorber/paraffin may change with the internal structural variation of absorbers (such as SSA, pore micromorphology and pore volume, etc.), leading to diverse formation of carbon-derived conductive network of different samples. All these factors contribute to the gradually increasing complex permittivity from PGCNs-0 to PGCNs-4. Similarly, the decrease complex permittivity of PGCNs-5 should be ascribed to the collapsed porous structure and the destroyed spherical structure. These results all confirm that the adjustment of microstructure on absorbers should be the reason for the fluctuation of the complex permittivity values.

With higher complex permittivity, PGCNs-3 and PGCNs-4 absorbers are supposed to exhibit stronger attenuation capability for EMW, which can be estimated by the attenuation constant α calculated as follows [36]:

$$\alpha = \frac{\sqrt{2}\pi f}{c}\sqrt{(\mu''\varepsilon'' - \mu'\varepsilon') + \sqrt{(\mu''\varepsilon'' - \mu'\varepsilon')^2 + (\mu'\varepsilon'' + \mu''\varepsilon')^2}} \tag{3}$$

As shown in Fig. 4a, PGCNs-3 and PGCNs-4 display much higher α than other samples, indicating their stronger attenuation capacity for EMW. However, the stronger attenuation capacity does not merely bond to excellent EMW absorbing property. The characteristic of impedance is another crucial factor for the absorbing property of absorbers, which means the ability for EMWs to enter the absorbers. The characteristic of impedance can be evaluated by $|Z_{in} - 1|$. When the $|Z_{in} - 1|$ is getting closer to 0, the better impedance matching can be obtained. The values of $|Z_{in} - 1|$ corresponding to the sample thickness of 2.2 mm were calculated and are exhibited in Fig. 4b. PGCNs-0 indicates the most mismatching impedance in all the samples. By contrast, PGCNs-3 shows the best impedance matching, whose $|Z_{in} - 1|$ is the closest to 0 than any other samples, indicating that the PGCNs-3 should possess better EMW absorbing property.

EMW absorbing property of absorbers is directly corresponding to the calculated RC. The effective absorption bandwidth (EAB) which means RC ≤ -10 dB ($\geq 90\%$ EMW was absorbed) and the minimum RC value (RC$_{min}$) are both key parameters to assess the EMW absorbing performance [20]. The EAB, RC$_{min}$, and RC values for all the obtained PGCNs are exhibited in Fig. 4c–l. PGCNs-0 exhibits the worst EMW absorbing performance, with the RC$_{min}$ of merely -4.28 dB at the thickness of 5 mm and is impossible for practical application. This result is consistent with its low attenuation constant and poor impedance matching. After the activation of KOH, PGCNs-2 shows a great enhancement on EMW absorbing performance, whose RC$_{min}$ and EAB come to -22.83 dB and 4.3 GHz; especially, the thickness corresponding to the widest EAB decreases to only 2.6 mm, manifesting the important role of activation. The best EMW absorbing performance appears on PGCNs-3. The EAB of PGCNs-3 comes to 6.3 GHz with the thickness of 2.2 mm; the RC$_{min}$ reaches -58.03 dB at the thickness of 1.9 mm, which is better than other samples. This superior EMW absorbing performance comes from the combined consequences of strong attenuation capacity and well-matched impedance. However, the RC$_{min}$ and EAB of PGCNs-4 show a declining tendency comparing with PGCNs-3, which is -43.81 dB and 4.5 GHz. With an almost similar attenuation constant with PGCNs-3, this delineation of PGCNs-4 might be caused by its slightly poorer impedance matching. Serious structural damage may result in the further mismatch impedance of PGCNs-5, simultaneously destroying the conductive network. The deteriorated dielectric loss and impedance match are the main reason for the weak EMW absorbing ability of PGCNs-5 with RC$_{min}$ of -22.48 dB and
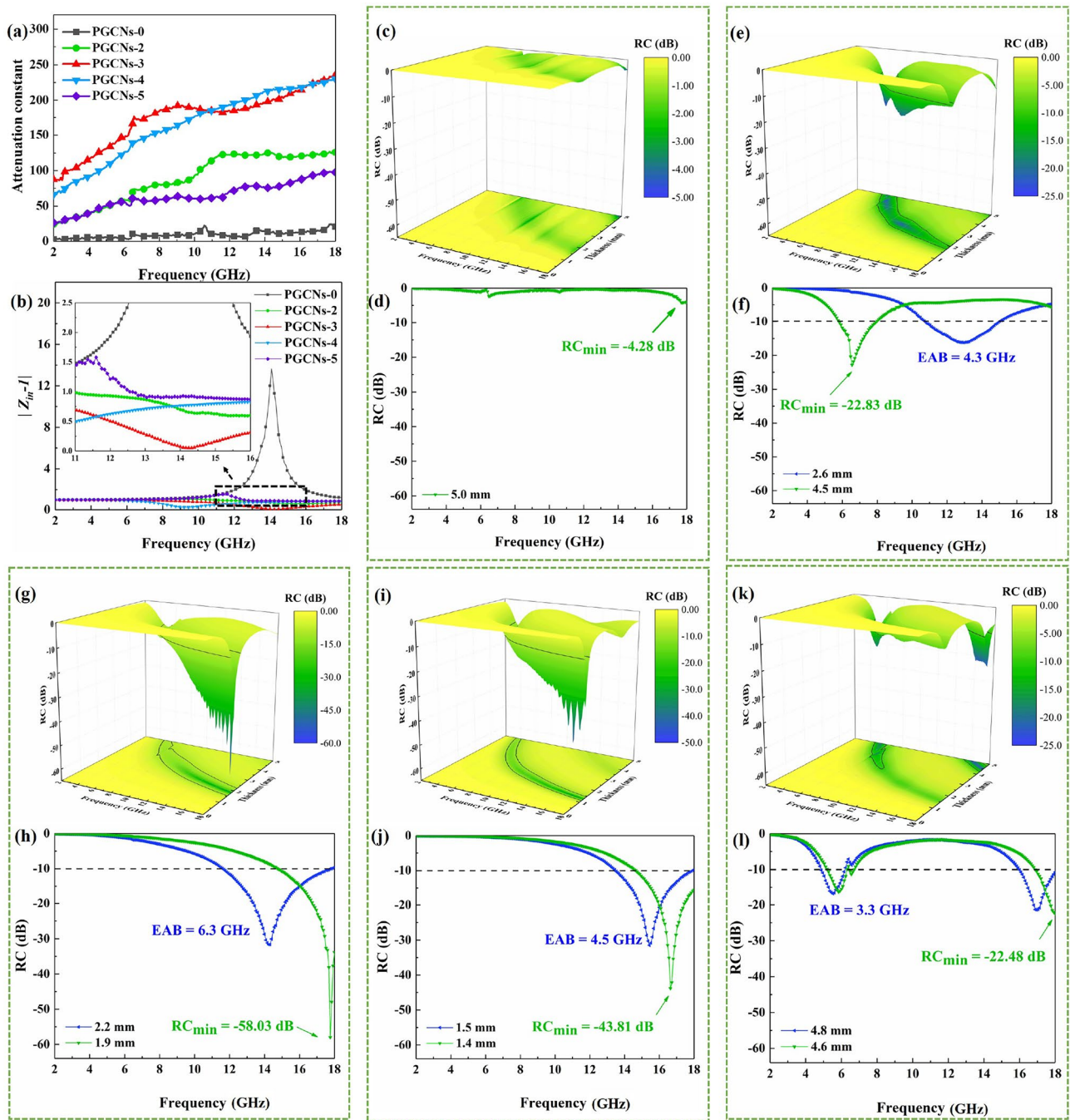
Fig. 4 **a** attenuation constant and **b** modulus of Z_{in}-1 (thickness = 2.2 mm) of PGCNs-0, PGCNs-2, PGCNs-3, PGCNs-4 and PGCNs-5; the minimum reflection coefficient, the effective band width and 3D color map images of reflection coefficient during 2–18 GHz for the **c**, **d** PGCNs-0, **e**, **f** PGCNs-2, **g**, **h** PGCNs-3, **i**, **j** PGCNs-4, and **k** ,**l** PGCNs-5, respectively

EAB of 3.3 GHz. A reasonable porous structure followed by proper KOH addition results in the higher RC value, which manifests the decisive role of structural adjustment in realizing excellent EMW absorbing property.

Figure 5 a shows the EAB with different sample thicknesses. The whole X and Ku band (8–18 GHz) could be completely covered by tuning the thickness to merely 3.0

and 2.2 mm, respectively. Based on the excellent EMW absorbing property of PGCNs-3, the change law of RC with frequency can be further studied with different thicknesses and its relationship with the quarter-wavelength (λ/4) matching model is illustrated in Fig. S2 [37, 38]. The EMW absorbing mechanisms can be further investigated according to Debye theory. The total loss (ε_t) of
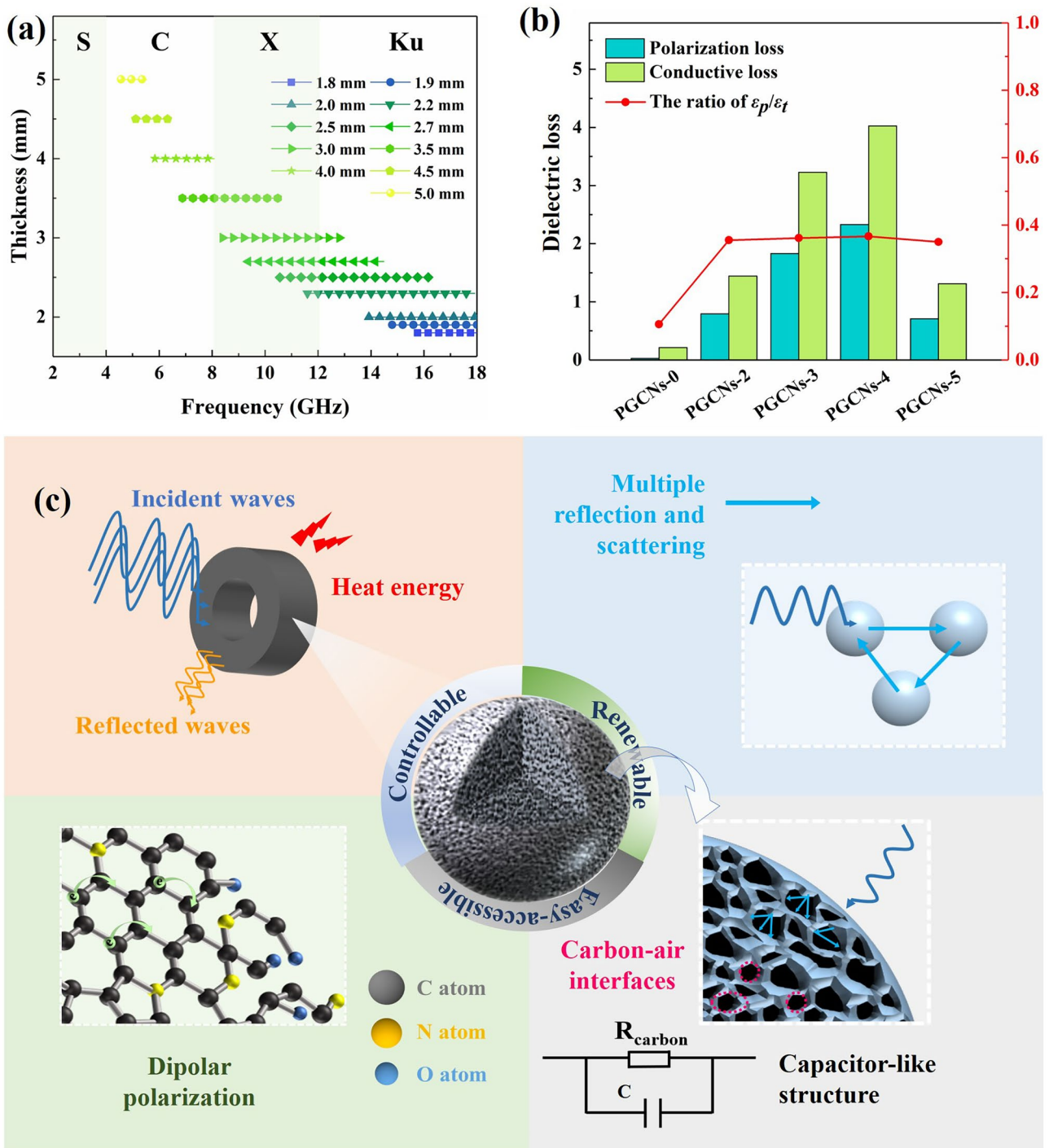
Fig. 5 **a** EAB of PGCNs-3 with different thickness. **b** Conductive loss and polarization loss of five samples. **c** The schematic of probable EMW absorbing mechanisms of PGCNs

carbonaceous absorbers can be divided into the polarization (ε_p) and conductive loss (ε_c). ε_p, ε_c, and the ratio of $\varepsilon_p/\varepsilon_t$ can be reliably fitted by the least-square method according to Eq. S1–4 [1, 14, 28, 39]. With the increasing ratio of GCNs/KOH from 1:0 to 1:4, the conductive loss,

polarization loss, and proportion of polarization loss synergistically intensify. Combined with both excellent attenuation ability and well-matched impedance, the PGCNs-3 sample shows the best EMW absorbing property. When the ratio comes to 1:5, all these parameters decrease because of the damaged structure and reveal the poor attenuation

Table 1 The comparison of RC_{min} and EAB between biomass carbon-based materials reported lately and PGCNs-3

Sample	RC_{min}/dB (Thickness/mm)	EAB/GHz (Thickness/mm)	Ref
K_2CO_3-PC	−76.0 (2.1)	5.9 (2.3)	[24]
BC/Fe_3O_4@C	−56.6 (2.5)	5.7 (1.5)	[44]
Porous carbon@$ZnFe_2O_4$	−54.1 (1.8)	5.8 (2.5)	[18]
Carbon-cotton /Co@NPC	−51.2 (1.65)	4.4 (1.65)	[45]
Hierarchical porous carbon/Co	−52.62 (2.6)	5.44 (1.9)	[46]
Graphene-like porous carbon nanosheet	−56.5 (2.3)	6.4 (2.3)	[47]
porous Co/C foam	−61.5 (2.03)	6.0 (2.49)	[43]
PGCNs-4	−43.81 (1.4)	4.5 (1.5)	This work
PGCNs-3	−58.03 (1.9)	6.3 (2.2)	This work

ability of PGCNs-5. A well-developed conductive network and more interface polarization can be induced by proper porous structure, indicating the significance on structural adjustment. Activation temperature is another significant factor for the final EMW absorbing property. The precursor GCNs were activated with triple KOH at 700 °C and 900 °C, which were denoted as PGCNs-3-700 and PGCNs-3-900. The morphology, pore properties, complex permittivity, and EMW absorbing performance were investigated and exhibited in Fig. S3-S4. A proper carbonization temperature also plays a vital role in the final EMW absorbing ability.

Based on the analysis above, the EMW absorbing properties of carbon nanospheres derived from gelatin can be significantly improved by tuning its porous structure with activation of KOH. The formation of large solid-air interfaces followed by the activation obviously promotes impedance matching, which is the precondition for EMW to enter the absorber [40, 41]. The synergistic effects of the multi-loss mechanisms of EMW absorbing for PGCNs-3 are illustrated in Fig. 5c. For carbon-derived material, conductive loss plays a leading role in all the mechanisms. With the formation of porous structure, a well-developed conductive network will be built through the carbon skeleton to induce conductive loss. Amorphous carbon can also be regarded as the resistance in the equivalent circuit model. Under alternating electromagnetic field, nanopores are equivalent to a micro-type capacitor-like circuit and contribute to the conductive loss. In addition, the defects and large interfaces between carbon and air give rise to the interfacial polarization; the remaining elements such as N, O atoms will act as the dipolar polarization center, both of which can effectively improve attenuation ability in the form of polarization loss. Lastly, the multiple reflection and scattering of EMW between absorbers and inside the nanopores will lengthen the propagation path, effectively increasing the possibility of being dissipated.

The RC_{min} and EAB of PGCNs in this work and other biomass-derived carbonaceous materials reported recently are listed in Table 1. The PGCNs-3 sample possesses superior EMW absorbing performance when compared with other biomass-derived carbonaceous materials which are even composited with metallic oxide or magnetic particles. In addition, EMW absorbing material using gelatin precursor reported recently such as porous carbon aerogel [42] and porous Co/C foam [43], inevitably encountered with the shortage of great thickness. The accurate morphology design in our work gave reduction to the thickness effectively while promoting the EMW absorbing performance. Possessing such superiority, as a single component material, PGCNs undoubtedly exhibit greater potential in future EMW absorbing fields if more research could be carried on in the future, such as studies on further optimizing structure and component.

4 Conclusion

In this work, gelatin-derived carbon nanospheres with tunable porous structure were firstly prepared successfully as EMW absorbers. With different KOH addition, the nanoporous structure of the absorber could be tuned, therefore influencing the final EMW absorbing performance. The porous nano-spherical structure with proper large specific area and pore volume was realized on PGCNs-3 by the constructed gelatin molecules and the assistance of activation, which contributes to the synergistic effect of various loss mechanisms and better-matched impedance. The PGCNs-3 sample (filler loading of only 15 wt.%) exhibited enhanced EMW absorption performance, with RC_{min} lower than −58.03 dB at the thickness of 1.9 mm and effective absorption bandwidth up to 6.3 GHz at the thickness of 2.2 mm. The prepared biomass-derived carbon material provided a simple synthesis strategy to construct fascinating geometry and

porous structure on biomass carbon, which might be adaptable in large-scale production and bringing enlightenment for further studies on carbonaceous absorbers.

Declarations

Conflict of interest The authors declare no competing interests.

References

1. Xu HL, Yin XW, Li MH, Ye F, Han MK, Hou ZX, Li XL, Zhang LT, Cheng LF (2018) Mesoporous carbon hollow microspheres with red blood cell like morphology for efficient microwave absorption at elevated temperature. Carbon 132:343–351

2. Kong L, Yin XW, Xu HL, Yuan XY, Wang T, Xu ZW, Huang JF, Yang R, Fan H (2019) Powerful absorbing and lightweight electromagnetic shielding CNTs/RGO composite. Carbon 145:61–66

3. Yousefi N, Sun XY, Lin XY, Shen X, Jia JJ, Zhang B, Tang BZ, Chan MS, Kim JK (2014) Highly aligned graphene/polymer nanocomposites with excellent dielectric properties for high-performance electromagnetic interference shielding. Adv Mater 26:5480–5487

4. Nan HY, Qing YC, Gao H, Jia HY, Luo F, Zhou WC (2019) Synchronously oriented Fe microfiber & flake carbonyl iron/epoxy composites with improved microwave absorption and lightweight feature. Compos Sci Technol 184:107882

5. Gu Z, Fang X, Liu T, Gao H, Liang S, Li Y, Liang B, Cheng J, Zhu J (2021) A reconfigurable active acoustic metalens. Appl Phys Lett 118:133502. https://doi.org/10.1063/5.0045024

6. Xie P, Liu Y, Feng M, Niu M, Liu C, Wu N, Sui K, Patil RR, Pan D, Guo Z et al (2021) Hierarchically porous Co/C nanocomposites for ultralight high-performance microwave absorption. Adv Compos Hybrid Mat. https://doi.org/10.1007/s42114-020-00202-z

7. Liu P, Gao S, Wang Y, Huang Y, Zhou F, Liu P (2021) Magnetic porous N-doped carbon composites with adjusted composition and porous microstructure for lightweight microwave absorbers. Carbon 173:655–666

8. Wang X, Pan F, Xiang Z, Zeng QW, Pei K, Che RC, Lu W (2020) Magnetic vortex core-shell Fe_3O_4@C nanorings with enhanced microwave absorption performance. Carbon 157:130–139

9. Liu QH, Cao Q, Bi H, Liang CY, Yuan KP, She W, Yang YJ, Che RC (2016) CoNi@SiO2@TiO2 and CoNi@Air@TiO$_2$ microspheres with strong wideband microwave absorption. Adv Mater 28:486–490

10. Zhou X, Jia Z, Feng A, Qu S, Wang X, Liu X, Wang B, Wu G (2020) Synthesis of porous carbon embedded with NiCo/CoNiO2 hybrids composites for excellent electromagnetic wave absorption performance. J Colloid Interf Sci 575:130–139

11. Lyu L, Wang F, Zhang X, Qiao J, Liu C, Liu J (2021) CuNi alloy/carbon foam nanohybrids as high-performance electromagnetic wave absorbers. Carbon 172:488–496

12. Deng ZH, He SR, Wang W, Xu MZ, Zheng HY, Yan JF, Zhang WX, Yun JN, Zhao W, Gan PY (2020) Construction of hierarchical SnO2@Fe3O4 nanostructures for efficient microwave absorption. J Magn Magn Mater 498:166224

13. Zhang W, Zhang X, Zhu Q, Zheng Y, Liotta LF, Wu H (2020) High-efficiency and wide-bandwidth microwave absorbers based on MoS2-coated carbon fiber. J Colloid Interf Sci 457–468.

14. Li MH, Yin XW, Xu HL, Li XL, Cheng LF, Zhang LT (2019) Interface evolution of a C/ZnO absorption agent annealed at elevated temperature for tunable electromagnetic properties. J Am Ceram Soc 102:5305–5315

15. Zhao H, Cheng Y, Lv H, Ji G, Du Y (2019) A novel hierarchically porous magnetic carbon derived from biomass for strong lightweight microwave absorption. Carbon 142:245–253

16. Shang Q, Feng H, Liu J, Lian Q, Feng Z, Chen N, Qiu J, Wu H (2021) Constructing and optimizing hollow ZnxFe3-xO4@polyaniline composites as high-performance microwave absorbers. J Colloid Interf Sci 584:80–91

17. Li X, Li MH, Lu XK, Zhu WJ, Xu HL, Xue JM, Ye F, Liu YS, Fan XM, Cheng LF (2021) A sheath-core shaped ZrO$_2$-SiC/SiO$_2$ fiber felt with continuously distributed SiC for broad-band electromagnetic absorption. Chem Eng J 419:129414

18. Di X, Wang Y, Fu Y, Wu X, Wang P (2021) Wheat flour-derived nanoporous carbon@ZnFe2O4 hierarchical composite as an outstanding microwave absorber. Carbon 173:174–184

19. Zhou XF, Jia ZR, Feng AL, Wang XX, Liu JJ, Zhang M, Cao HJ, Wu GL (2019) Synthesis of fish skin-derived 3D carbon foams with broadened bandwidth and excellent electromagnetic wave absorption performance. Carbon 152:827–836

20. Xu H, Yin X, Li Z, Liu C, Wang Z, Li M, Zhang L, Cheng L (2018) Tunable dielectric properties of mesoporous carbon hollow microspheres via textural properties. Nanotechnology 29:184003

21. Coester CJ, Langer K, Von Briesen H, Kreuter J (2000) Gelatin nanoparticles by two step desolvation - a new preparation method, surface modifications and cell uptake. J Microencapsul 17:187–193

22. Xiang Z, Xiong J, Deng B, Cui E, Yu L, Zeng Q, Pei K, Che R, Lu W (2020) Rational design of 2D hierarchically laminated Fe_3O_4@nanoporous carbon@rGO nanocomposites with strong magnetic coupling for excellent electromagnetic absorption applications. J Mat Chem C 8:2123–2134

23. Cui J, Zhou Z, Jia M, Chen X, Shi C, Zhao N, Guo X (2020) Solid polymer electrolytes with flexible framework of SiO(2)nanofibers for highly safe solid lithium batteries. Polymers 12:1324

24. Zhou X, Jia Z, Feng A, Wang K, Liu X, Chen L, Cao H, Wu G (2020) Dependency of tunable electromagnetic wave absorption performance on morphology-controlled 3D porous carbon fabricated by biomass. Compos Commun 21:100404

25. Xu H, Yin X, Zhu M, Han M, Hou Z, Li X, Zhang L, Cheng L (2017) Carbon hollow microspheres with a designable mesoporous shell for high-performance electromagnetic wave absorption. ACS Appl Mater Interfaces 9:6332–6341

26. Gao H, Ding L, Bai H, Liu A, Li S, Li L (2016) Pitch-based hyper-cross-linked polymers with high performance for gas adsorption. J Mat Chem A 4:16490–16498

27. Wu Z, Tian K, Huang T, Hu W, Xie F, Wang J, Su M, Li L (2018) Hierarchically porous carbons derived from biomasses with excellent microwave absorption performance. ACS Appl Mater Interfaces 10:11108–11115

28. Li M, Fan X, Xu H, Ye F, Xue J, Li X, Cheng L (2020) Controllable synthesis of mesoporous carbon hollow microsphere twined by CNT for enhanced microwave absorption performance. J of Mat Sci Tech 59:164–172

29. Liu X, Culhane C, Li W, Zou S (2020) Spinach-derived porous carbon nanosheets as high-performance catalysts for oxygen reduction reaction. ACS Omega 5:24367–24378

30. Zhou X, Jia Z, Feng A, Kou J, Cao H, Liu X, Wu G (2020) Construction of multiple electromagnetic loss mechanism for

enhanced electromagnetic absorption performance of fish scale-derived biomass absorber. Compos Pt B-Eng 192:107980

31. Yao QF, Wang HW, Wang C, Jin CD, Sun QF (2018) One step construction of nitrogen-carbon derived from bradyrhizobium japonicum for supercapacitor applications with a soybean leaf as a separator. Acs Sustain Chem Eng 6:4695–4704

32. Xu H, Yin X, Zhu M, Li M, Zhang H, Wei H, Zhang L, Cheng L (2019) Constructing hollow graphene nano-spheres confined in porous amorphous carbon particles for achieving full X band microwave absorption. Carbon 142:346–353

33. Du Y, Liu W, Qiang R, Wang Y, Han X, Ma J, Xu P (2014) Shell thickness-dependent microwave absorption of core-shell Fe3O4@C composites. ACS Appl Mater Interfaces 6:12997–13006

34. Lv H, Li Y, Jia Z, Wang L, Guo X, Zhao B, Zhang R (2020) Exceptionally porous three-dimensional architectural nanostructure derived from CNTs/graphene aerogel towards the ultra-wideband EM absorption. Compos Pt B-Eng 196:108122

35. Zhao H, Cheng Y, Lv H, Zhang B, Ji G, Du Y (2018) Achieving sustainable ultralight electromagnetic absorber from flour by turning surface morphology of nanoporous Carbon. Acs Sustain Chem Eng 6:15850–15857

36. Liu PB, Gao S, Wang Y, Huang Y, He WJ, Huang WH, Luo JH (2020) Carbon nanocages with N-doped carbon inner shell and Co/N-doped carbon outer shell as electromagnetic wave absorption materials. Chem Eng J 381:122653

37. Zhou PP, Wang XK, Wang LX, Zhang J, Song Z, Qiu X, Yu MX, Zhang QT (2019) Walnut shell-derived nanoporous carbon@Fe3O4 composites for outstanding microwave absorption performance. J Alloy Compd 805:1071–1080

38. Li J, Xie Y, Lu W, Chou T-W (2018) Flexible electromagnetic wave absorbing composite based on 3D rGO-CNT-Fe3O4 ternary films. Carbon 129:76–84

39. Zhu W, Ye F, Li M, Wang X, Zhou Q, Fan X, Xue J, Li X (2020) In-situ growth of wafer-like Ti3C2/Carbon nanoparticle hybrids with excellent tunable electromagnetic absorption performance. Compos Pt B-Eng 202:108408

40. Song P, Liu B, Liang C, Ruan C, Qiu H, Ma Z, Guo Y, Gu J (2021) Lightweight, flexible cellulose-derived carbon aerogel@reduced graphene oxide/PDMS composites with outstanding EMI shielding performances and excellent thermal conductivities. Nano-Micro Lett 13:91

41. Song P, Qiu H, Wang L, Liu X, Zhang Y, Zhang J, Kong J, Gu J (2020) Honeycomb structural rGO-MXene/epoxy nanocomposites for superior electromagnetic interference shielding performance Sustain Mater Techno 24:e00153

42. Liu P, Gao S, Chen C, Zhou F, Meng Z, Huang Y, Wang Y (2020) Organic polymer aerogel derived N-doped carbon aerogel with vacancies for ultrahigh microwave absorption. Carbon 169:276–287

43. Huang T, Wu Z, Lin J, Yu Q, Tan D, Li L (2019) A facile freeze-drying strategy to prepare hierarchically porous co/c foams with excellent microwave absorption performance. ACS Appl Electro Mat 1:2541–2550

44. Li Z, Lin H, Ding S, Ling H, Wang T, Miao Z, Zhang M, Meng A, Li Q (2020) Synthesis and enhanced electromagnetic wave absorption performances of Fe3O4@C decorated walnut shell-derived porous carbon. Carbon 167:148–159

45. Zhao HQ, Cheng Y, Ma JN, Zhang YN, Ji GB, Du YW (2018) A sustainable route from biomass cotton to construct lightweight and high-performance microwave absorber. Chem Eng J 339:432–441

46. Liu TS, Liu N, Gai LX, An QD, Xiao ZY, Zhai SR, Cai WJ, Wang HS, Li ZC (2020) Hierarchical carbonaceous composites with dispersed Co species prepared using the inherent nanostructural platform of biomass for enhanced microwave absorption. Microporous Mesoporous Mat 302:110210

47. Zhao H, Cheng Y, Zhang Z, Zhang B, Pei C, Fan F, Ji G (2020) Biomass-derived graphene-like porous carbon nanosheets towards ultralight microwave absorption and excellent thermal infrared properties. Carbon 173:501–511

48. Liu PB, Sai Gao, Chen C, Zhou FT, Meng ZY, Huang Y, Wang Y, (2020) Vacancies-engineered and heteroatoms-regulated N-doped porous carbon aerogel for ultrahigh microwave absorption. Carbon 169:276–287